**RESEARCH PAPER**

# Thermodynamic prediction of precipitations behaviour in HAZ of a gas metal arc welded S690QL with varying Ti and Nb content

Nina Schroeder[1] · Michael Rhode[1,2] · Thomas Kannengiesser[1,2]

## Abstract

For a significant increase in the strength of high-strength fine-grained structural steels with a nominal yield strength ≥690 MPa, the addition of microalloying elements such as Nb and Ti is required. The standard specifications for the chemical composition of these steels (e.g., in EN 10025-6) often only give the manufacturer limit contents to achieve the defined properties. The effect of the alloying elements in the heat affected zone (HAZ) is sometimes completely contrary. This makes it difficult to adequately predict the batch dependency regarding weldability and the load-bearing behaviour of the welded joint. Three different micro-alloyed steels of the grade S690QL were produced on a laboratory scale, focusing on different Nb and Ti contents. To investigate the tempering effect, these were gas metal arc welded in three layers. In addition to metallographic investigations of individual HAZ areas, thermodynamic phase calculations were carried out using Thermo-Calc, following variations in the chemical composition. This provides an understanding of phase transformation, precipitation growth, and dissolution during welding as a function of temperature and cooling conditions. The results show a divergent metallurgical behaviour in the HAZ of the three different micro-alloyed steels. Thereby, the Ti micro-alloyed grade showed a strong softening of the HAZ in contrast to the Nb micro-alloyed grade. This can be attributed to a contrary precipitation behaviour during welding.

**Keywords** High-strength structural steel · Gas metal arc welding · HAZ-softening · Microalloying influences · Thermodynamic simulation

## 1 Introduction

The economic and environmental benefits of using micro-alloyed high strength low-alloyed (HSLA) steels depend on the use of highly productive welding processes, suitable filler metals, and an appropriate weld configuration. Therefore, a fundamental understanding of the influence of modern welding processes on the microstructure changes during welding and the corresponding mechanical properties is

necessary [1]. Lightweight design in steel construction requires the increasing use of high-strength structural steels with yield strengths ≥690 MPa [2, 3]. The focus in the use of high-strength fine-grained structural steels lies on maximising the load-bearing capacity with low dead weight, whereby the challenges in the welding processing of these steels increase with the increasing strength. To achieve the required mechanical properties of the welded structure, it is crucial to select an appropriate filler material as well as a suitable thermal input (heat input, preheating, and interpass temperature) is of decisive importance. The mechanical properties of a welded joint are determined by the weld metal (WM) and the heat-affected zone (HAZ). Microalloying concepts with specific Ti and Nb additions are therefore indispensable for high-strength welded joints. The increase in strength results from grain refinement increased precipitation hardening and the increase in dislocation density [4]. It is well known that in the case of welding of high-strength steel, when the tempering temperature is reached in the initial structure, diffusion of carbon from the C-supersaturated

✉ Nina Schroeder
  nina.schroeder@bam.de

1  Bundesanstalt für Materialforschung und -prüfung (BAM), Department 9 - Component Safety, Division 9.4 - Weld Mechanics, Unter den Eichen 87, 12205 Berlin, Germany

2  Otto-von-Guericke University Magdeburg, Institute for Materials Science and Joining Technology, Universitätsplatz 2, 39106 Magdeburg, Germany

martensite often occurs. The result is carbide coarsening, carbide coagulation, or recrystallisation of the grains. These carbide reactions can also occur in a martensite-bainite mixture (in quenched and tempered/QT condition) if tempering is conducted at a peak temperature below $A_{c1}$ for a certain dwell time [5]. The same behaviour is seen in high-strength martensitic-ferritic dual phase (DP) steels with high martensite phase fraction [6–8]. The alloying concepts of HSLA steels and the corresponding weld filler metals differ with respect to the manufacturer. Current standards like EN 10025-6 [9] only provide ranges or maximum tolerable additions of alloy elements to the chemical composition. The weldability concerning the mechanical properties of the welded joint change significantly even with small differences in the amount of Nb and Ti as micro-alloy element [10, 11]. High-performance welding processes, such as GMAW with modified spray arc, are characterised by their high heat input [12]. This can result in localised softening as well as to the opposite effect of hardening in the HAZ [13]. The metallurgical factors for the specific softening mechanism in the individual subzones of the HAZ (like fine and coarse-grained or intercritical zone) are not yet fully understood. Multi-layer welded joints made of high-strength fine-grained structural steels can exhibit both softening and hardening in the HAZ because of unfavourable welding heat conduction (tempering effects). To ensure the integrity of a welded component made of high-strength structural steels, it is necessary to analyse the effect of precipitation behaviour and phase transformation products in welded joints. It is of importance to acquire knowledge about the influence of different micro-alloy routes to the undesirable effects in the HAZ, such as softening and/or hardening.

## 2 Materials and methods

### 2.1 Materials

For the investigation of the microalloying routes, three different laboratory melts were investigated as base materials (BM). They had a thickness of 15 mm and were quenched and tempered in accordance with [9] (kindly delivered by voestalpine (Grobblech GmbH, Linz, Austria) in accordance and conform to a steel grade S690Q. A solid filler wire (Ø 1.2 mm) was used for the WM deposition. The strength class corresponds to a conventionally and commercially available G69 filler wire (according to ISO 16834) [14]. Table 1 shows the chemical composition of the three different investigated BMs and the pure WM in deposited condition. In that connection, the Ti- and Nb-free S690Q is further labelled as "reference," "A" represents the Nb-alloyed grade, and "B" the Ti-alloyed grade.

Figure 1 shows the scanning electronic micrographs in secondary electron detector (SED) mode of the three BMs

**Table 1** Chemical composition in wt.-% of test materials (Fe - balance)

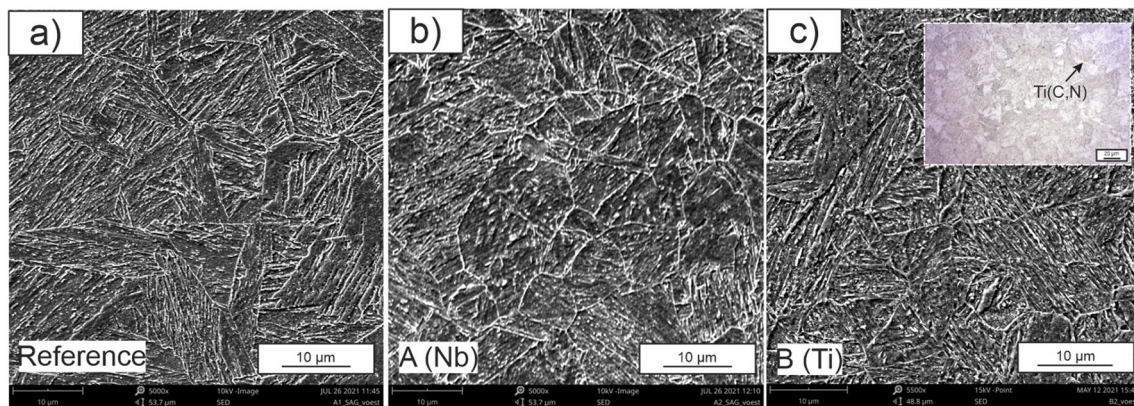| Material | C | Si | Mn | Cr | Mo | Al | Nb | Ti | N |
|---|---|---|---|---|---|---|---|---|---|
| BM: **Reference** | 0.086 | 0.3 | 1.68 | 0.17 | 0.31 | 0.11 | _ | _ | 0.0063 |
| BM: Grade **A (Nb-alloyed)** | 0.085 | 0.3 | 1.68 | 0.17 | 0.31 | 0.11 | 0.026 | _ | 0.0065 |
| BM: Grade **B (Ti-alloyed)** | 0.085 | 0.3 | 1.61 | 0.17 | 0.31 | 0.1 | _ | 0.017 | 0.0056 |
| WM: **G69** Ø 1.2 mm | 0.09 | 0.43 | 1.32 | 0.2 | 0.55 | 0.002 | 0.001 | 0.019 | 0.007 |



**Fig. 1** SEM micrographs of the base materials (secondary electron detector mode): **(a)** reference, **(b)** A (Nb-microalloyed), and **(c)** B (Ti-microalloyed)

investigated, acquired with the SEM "Phenom XL" (from Thermo Fisher Scientific, Germany) (and the light microscope image in Fig. 1c with the light microscope "Polyvar Met" (from Reichert-Jung, Germany) and the associated acquisition software "IMS Client" (from Imagic, Germany). The respective sample preparation steps are described in detail in Section 2.3.

All three steels have a bainitic-martensitic microstructure, which is characterised by an acicular morphology. The nucleation is located at the previous austenite grain boundaries with the same spatial orientation and numerous fine precipitates between the needles. In grade B (Ti-microalloyed), the shape characteristic of Ti inclusions (yellow, angular appearance, see Fig. 1c: light microscope image) is clearly visible in the bainitic-martensitic grains and along the grain boundaries. These optical visible large Ti inclusions are due to the steel manufacturing process during the molten phase. The mean grain diameter is characterised by the linear intercept method, stated as average and standard deviation: reference: $(15.7 \pm 1.4)$ µm, A (Nb-microalloyed): $(13.4 \pm 0.8)$ µm, and B (Ti-microalloyed): $(12.2 \pm 1.2)$ µm. For these, the number of objects measured varied between 129 and 206, and the Vickers hardness (Reference: $(279 \pm 6)$ HV1, A (Nb-microalloyed): $(284 \pm 8)$ HV1, and B (Ti-microalloyed): $(287 \pm 6)$ HV1) of the three BMs is almost identical.

## 2.2 Welding experiments

Three-layer welds were used for the 15-mm-thick plates in PA position using GMAW. The influence of heat transfer from the test set-up to the welding test sheets via free convection was minimised using some remedial measures. For welding, the GMAW with active shielding gas, i.e., MAG, was used with the modified spray arc was. The shielding gas used was an M21 active shielding gas according to ISO 14175 [16], with 82 % Ar and 18 % $CO_2$. The welding speed for all three layers was set constant to 400 mm/min. The heat input was varied via the wire feed speed, which was 8 m/min for the root layer, 8.5 m/min for the

filler layer, and 9.5 m/min for the top layer. The DC welding parameters ranged from 262 A to 280 A and 24 V to 26 V. The average heat input was 1 kJ/mm and the average $t_{8/5}$-time (measured by laser pyrometer was 7.7 s). The preheating and interpass temperature were 100 °C. To monitor the cooling conditions after welding, four type K thermocouples were used each on the top side of the specimen and on the root side (see Fig. 2a and b). The weld seam opening angle was 30° (see Fig. 2c), and the weld seam length was 300 mm.

## 2.3 Sample preparation and hardness measurement

Samples for metallographic investigations were cut from the welded sheet transverse to the welding direction. These were embedded, ground, and polished to 1 µm with diamond suspension and etched with 2 % Nital for 10 s to 15 s. When the specimens are prepared for scanning electron microscopy, the time will extend to around 20 s. To estimate the hardness distribution in the weld, surface hardness measurements were carried out on cross-section samples using the UCI (Ultrasonic contact impedance) method (ISO 50159-1 [15]). The hardness indents were carried out on ground, polished, and etched samples following a hardness scanner UT-200 from BAQ GmbH. The loading force was 4.903 N (HV0.5), whereby the indentations were set at 0.2 mm (in $x$ and $y$ direction) and with a dwell time of 0.5 s. Furthermore, for quantitative statement about the softening behaviour of the three-layer welds, HV1 Vickers (ISO 6507-1 [17]) rows were set in each layer. A schematic diagram of the position and distance of the hardness indentations is shown in Fig. 3 (green lines are measuring lines). Subsequently, the maximum softening ratio $R_{max.Soft}$ was determined for each layer according to the equation (1), which describes the percentage decrease in hardness in the HAZ in relation to the maximum hardness in the heat unaffected base metal.



**Fig. 2** Welding set-up: **(a)** positioning of the type-K thermocouples, top side (arrangement root side mirrored), **(b)** test set-up for welding tests (WD, welding direction), and **(c)** illustration of seam layer set-up of a three-layer weld
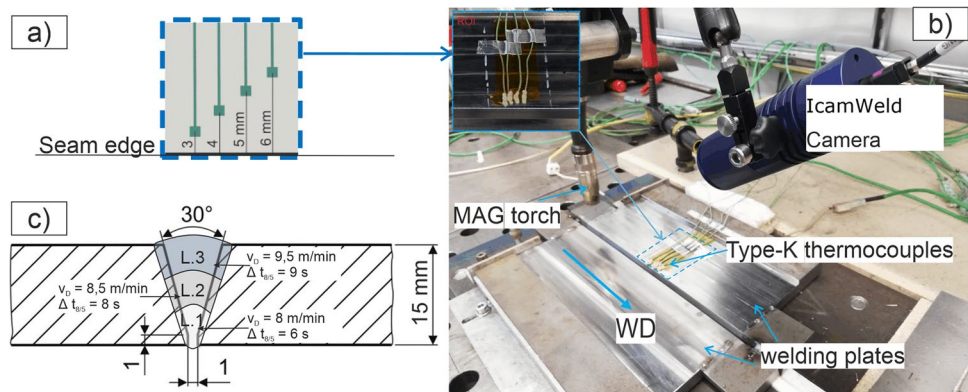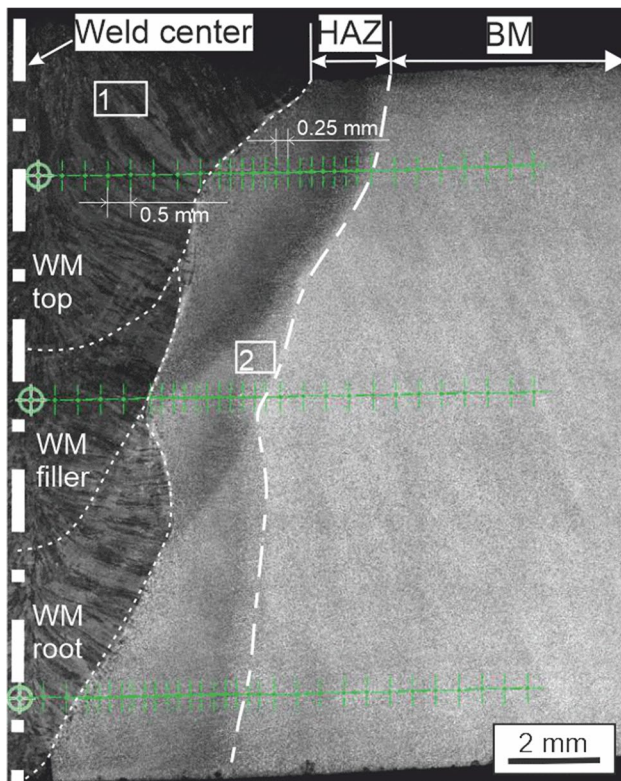
**Fig. 3** Schematic illustration of the positions of the hardness indentations (green lines) to determine the softening behaviour respectively the softening ratio and the regions of image acquisition, marked by frame 1: weld metal and frame 2: the ICHAZ regions of the filler layers

$$R_{\max.\text{Soft}} = \left(1 - \frac{\min.\text{HV1}_{\text{HAZ}}}{\max.\text{HV1}_{\text{BM}}}\right) \times 100\% \tag{1}$$

where min. HV1$_{\text{HAZ}}$ is the locally measured minimum HV1 hardness in the HAZ, and max. HV1$_{\text{BM}}$ is the locally measured maximum HV1 hardness in the heat unaffected base material (see Fig. 3; the green lines are hardness indentations along each layer). Therefore, the region of the lowest hardness corresponds to the maximum softening rate and the most severe softening behaviour of the joint.

### 2.4 Thermodynamic simulation of the precipitation behaviour

Complementary to the experimental investigations, thermodynamic modelling was carried out using the software Thermo-Calc©, version 2022b (simulation of equilibrium phase diagrams) [18] and application of the add-on module TC-PRISMA (simulation of precipitation behaviour under thermodynamic non-equilibrium, both from Thermo-Calc Software AB, Sweden). In the present work, the iron database "TCFE11" and the kinetics database "MOBFE6" were used.

If a system of several substances is defined that can form different phases, the energetic minimum (minimisation of the free Gibbs energy) of this system is searched for, which corresponds to the equilibrium state. The TC-PRISMA module allows modelling of nucleation [19], growth, and coarsening of dispersed particles following the numerical application of the CALPHAD method [20]. To determine the existence ranges and limits of the equilibrium phase stability, phase diagrams were calculated for the three different BMs (all alloying elements from Table 1) as a function of the phase volume fraction (total system size = 1 mol) and the temperature (between 500 °C and 1600 °C). This provided fundamental insights into the differences between the materials regarding their precipitation behaviour in the equilibrium state. To map the precipitation behaviour under the non-isothermal or non-equilibrium conditions during welding, further calculations were carried out in the TC-PRISMA module by implementing the measured temperature-time curves. Thus, in silico metallurgical processes occurring during the welding process can be numerically calculated and evaluated.

## 3 Results and discussion

### 3.1 Hardness

The HV0.5 hardness distribution of all welds determined by UCI is shown in Fig. 4. For that reason, the left part of the sub-parts (a) to (c) show the measured hardness and the right side shows the corresponding cross-sections, whereas the three-layer technique is clearly visible. All three investigated alloys show a significant hardness reduction in the intercritical HAZ (ICHAZ) and subcritical HAZ (SCHAZ). The intention of the UCI hardness mappings was to give a qualitative measure to summarise the complex metallurgical changes in the different subzones of the WEZ, such as the ICHAZ. For that purpose, the terms "softening" and "hardening" are used in the following to describe the changes in the hardness of the respective microstructure. Both softening or hardening are referred to the BM hardness of the corresponding steel grade in Table 1. The hardness reduction, respectively, the softening zone, can be recognised by the blue coloured area, see Fig. 4 and the corresponding legend on the right. Interestingly, a significant hardening occurs at the same time (400 to 450 HV0.5) in the coarse-grained HAZ (CGHAZ), see red shaded areas in Fig. 4a–c) of the last layer due to the missing further tempering.

The microstructure of the CGHAZ of the root and subsequent layers and that of the underlying layer of the WM is very refined by the doubled recrystallisation during heating and cooling. Thus, the hardness is reduced by the tempering effects that occur in multi-layer welding.in the
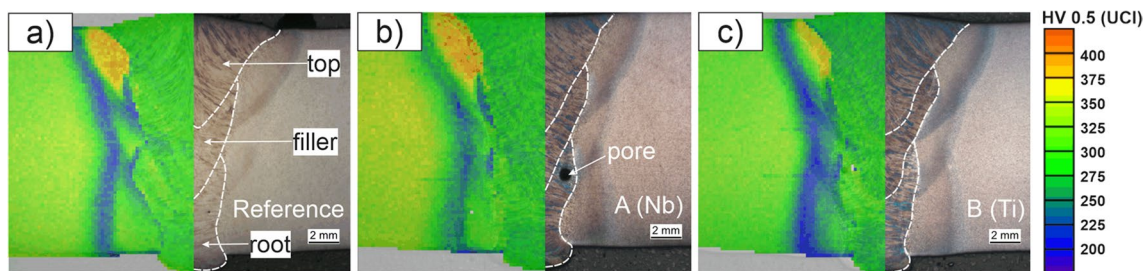
**Fig. 4** Hardness distribution (determined by UCI): **(a)** reference grade, **(b)** grade A (Nb-microalloyed), and **(c)** grade B (Ti-microalloyed) S690QL (dashed lines in micrographs indicate the fusion lines)

ICHAZ, SCHAZ, and in the WM. The reference grade shows a strongly pronounced softening effect not only in the outer HAZ areas but also directly along the fusion lines. Alloy A (Nb-microalloyed) shows moderate HAZ softening, with less pronounced softening in the outer HAZ regions of the top layer than in the filler and root layers. This can be explained by the lack of a tempering effect or the absence of heat from the subsequent layers. In addition, grade A (Nb-microalloyed) shows a wide hardening zone of the top layer compared to grade B (Ti-microalloyed). Hardness between 350 HV0.5 (UCI) and 400 HV0.5 (UCI) is found in this hardening zone. Furthermore, grade B (Ti-microalloyed) shows significant softening in the outer HAZ regions. To identify these significant differences between different microalloyed S690QL, microstructure characterisation investigations were carried out using SEM/EDX.

Figure 5a shows three HV1 hardness distributions of the top layer from the weld centre across, HAZ and BM for all investigated alloys. The different BM had a comparable average hardness of 281 to 331 HV1. In the HAZ, the hardness increases to a maximum for all three alloys, which is between 346 and 349 HV1. Due to the high

peak temperatures greater than 1200 °C and high cooling rates ($\Delta t_{8/5}$ time at 9 s) measured at the weld seam edge respectively in the CGHAZ, the steel exhibits complete austenitisation. Fast grain growth takes place due to the dissolution of carbides and nitrides, depending on their thermal stability. This causes a coarse-grained microstructure which, depending on the carbon equivalent, consists of martensite and or bainite. Thus, the hardening in the CGHAZ of the top layer can be explained [21–23]. Furthermore, a significant softening can be seen in the ICHAZ and SCHAZ of the top layer. This area corresponds to the blue band in Fig. 4 (UCI hardness measurements). This area is affected by measured peak temperatures of over 690 °C, which corresponds to partial austenitisation and a tempering process of the microstructure. This results in a new formation of the microstructure with a different phase distribution consisting of a multi-phase structure and a higher ferrite fraction than that of the base material, which in turn leads to softening. This area shows a hardness within a range from 242 to 288 HV1, which would mean a hardness reduction, or softening ratio of 26.8%, compared to the specifically designed base alloys (see
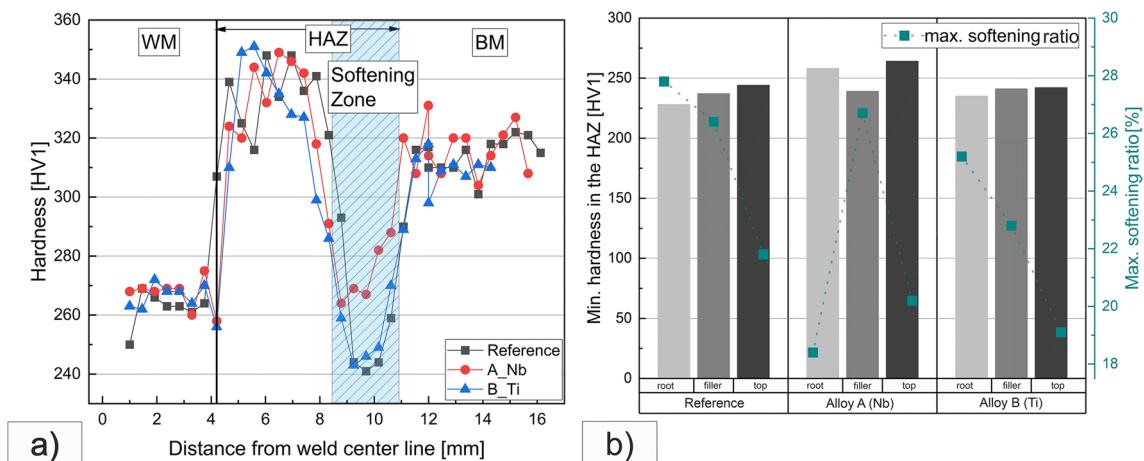


**Fig. 5** **(a)** HV1 hardness distribution in the top layer and **(b)** minimum HAZ hardness HV1 of individual layers for each grade and maximum softening rate

Table 1). The hardness distribution in the WM is between 260 and 287 HV1.

Figure 5b presents the minimum hardness HV1 in the HAZ for both each layer and the respective alloy type. In addition, the maximum softening rate ($R_{\text{max.Soft}}$) was determined for each layer. The softening rate is defined as the percentage of reduced hardness compared to the maximum hardness in the BM. The minimum hardness HV1 decreases from the top layer to the root layer, as expected due to the tempering effect. This can be clearly identified by the softening rate. The softening rate is highest in the filler and root layers (28 to 23 %).

These results indicate a strong tempering effect. Peak temperatures between 600 °C and $A_{c1}$ temperature, occurring in the SCHAZ region, reduce both the hardness and strength of these steels. The causes of hardness reduction are coarsening of precipitates, healing of defect structures by crystal recovery and recrystallisation (dissolution of the needled martensite structure into ferrite crystals) [24, 25].

## 3.2 Microstructure

Figure 6 shows a selected area of the WM microstructure. As mentioned in Section 2.1, the same filler metal was used in for the welding experiments. The WM microstructure (Fig. 6a) consists of acicular ferrite, which is oriented intragranular from inclusions. Based on the low $t_{8/5}$ -time of 9 s of the WM, it can be assumed that, as an effect of the high peak temperature and depending on the chemical composition of the WM, retained austenite or martensite-austenite constituents are present between the ferrite plates. EDX analysis (Fig. 6b) on an inclusion identified in the WM (Fig. 6a marked with white arrows) showed that this is a complex, oxidic compound of Al, Ti, and Mn. Ti-rich oxides or nitrides in combination with Al-rich oxides or manganese sulphides (MnS) are preferred nucleation sites for acicular ferrite [26].

In addition, SEM micrographs of the SCHAZ of the filler layers (in accordance with Fig. 3, marks with the rectangle 2) for each grade are shown in Fig. 7. This area is characterised by doubled tempering caused by three-layer welding technique. Observations of the microstructure at softened



**Fig. 7** SEM micrographs (back-scattered electron mode) of the SCHAZ of the filling layers and corresponding EDX spectra: **(a)** reference grade, **(b)** grade A (Nb-microalloyed), and **(c)** grade B (Ti-microalloyed)

HAZ suggest that partial phase transformation happened in the three SCHAZ but the transformation products differ significantly amongst them. The recorded temperature-time curves during welding suggest typical peak temperatures of max. 690 °C in these areas. In the sub-figures a to c, the microstructures are shown on the left-hand side, whereas "F" indicates the ferrite and "M" the tempered martensite/bainite and exemplary EDX-spectra are shown on the right-hand side.

The high peak temperatures of 690 °C exceed the tempering temperature of the BM (between 560 °C and 660 °C) [27], whereby carbides can precipitate from the martensitic solid solution, forming clusters. This causes low hardness, reduced strength, and toughness in this range [28]. The SEM micrographs (Fig. 7a–c) show a tempered microstructure

**Fig. 6** **(a)** SEM micrographs (back-scattered electron mode) of WM (inclusions are marked by white arrows) and **(b)** representative EDX spectrum of one inclusion (marked by blue arrow in figure a)
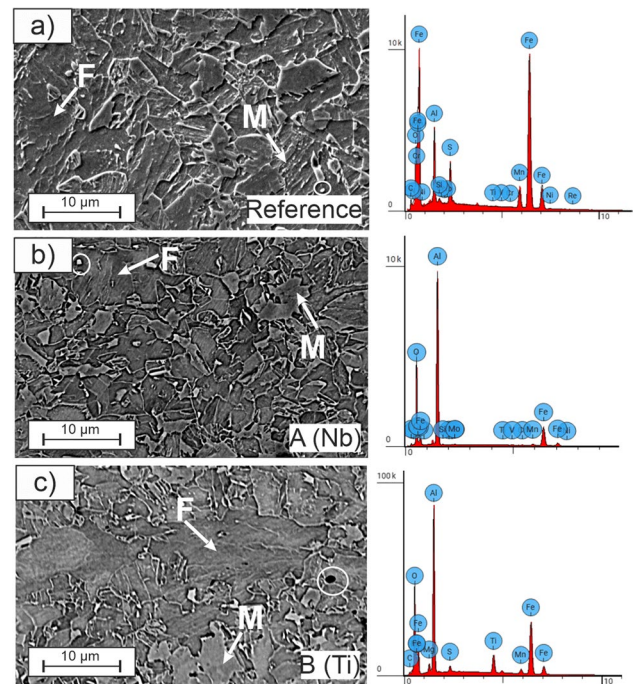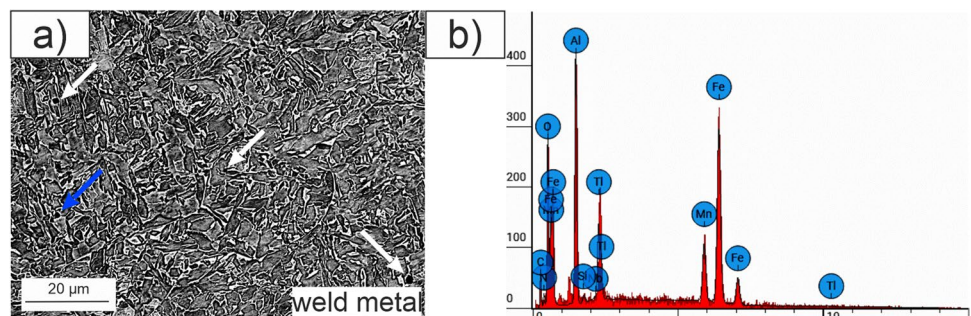
consisting of tempered martensite with precipitated carbides, which differs between the three alloys investigated. As indicated in Fig. 7a–c, the ferrite phase dimension seems to differ between the three steel grades investigated. The ferrite phase dimension appears to be higher in grade B (Ti-microalloyed) than in the other two grades. Supporting grain size measurement was not undertaken due to the limited information of a grain diameter quantification in μm as the HAZ grain size distribution is very complex, especially in multi-layer weld joints. From that point of view, we just give a qualitative statement. Furthermore, the ferrite phase dimension is much larger in the Ti-microalloyed steel, which in turn would explain the lower hardness of the outer HAZ regions in the grade B (Ti-microalloyed). Furthermore, small amounts of tempered martensite and bainite are also visible. Grade A (Nb-microalloyed) appears to have a higher concentration of these structures, which makes the steel more resistant to severe softening [28]. There are different metallurgical theories that can explain why an alloy with Nb at annealing temperatures of 450 °C–600 °C has a delayed reduction in hardness. The mechanism corresponding to the study is the secondary hardening during the tempering process through the precipitation of secondary carbides. Especially Mo in combination with Nb prevents a strong softening at tempering temperatures.

As all three steels contain relatively high amounts of aluminium (see Table 1), the typical effect as grade element is to act as deoxidiser and as precipitation hardener [29, 30]. Complex aluminium precipitates were found in these areas by EDX. The addition of Al binds the residual oxygen to $Al_2O_3$ and the atomic nitrogen to AlN. Nitrogen bonding reduces the effect of deformation ageing and improves low-temperature toughness and increases brittle fracture resistance. AlN precipitates as excellent nuclei reduce the secondary grain size of the ferrite, which positively influences the deformation capacity and impact strength of the steel [23].

## 3.3 Thermodynamic simulations

### 3.3.1 Phase diagrams under equilibrium conditions (Thermo-Calc)

The thermodynamic simulation of the phase diagrams under equilibrium conditions was carried out for the investigated materials with the alloying elements listed in Table 1. The corresponding phase diagrams are shown in Fig. 8. All alloys showed similar phase transformation behaviour. For example, $A_{c1}$ temperatures were around 680 °C, $A_{c3}$ around 840 °C, and the solidus temperature around 1480 °C. The relevant findings of the simulation are the calculated temperatures of the respective precipitates as a function of the microalloying concept.

The reference alloy (Fig. 8a) only shows AlN precipitates, which precipitate in the ferritic matrix from about 1200 °C during cooling. Congruently, AlN also precipitates in the grade A (Nb-microalloyed), followed by NbC at around 1100 °C (Fig. 8b). In contrast, the grade B (Ti-microalloyed), shown in Fig. 8c, had a completely different precipitation behaviour. Thus, Ti(C,N) forms precipitates at temperatures above 1480 °C as well. AlN precipitates are also formed in grade B (Ti-microalloyed) steel, but its precipitation temperature (1060 °C) decreases and the volume fraction in the matrix decreases. Therefore, the high thermal stability of the Ti precipitates can be proven numerically. It is known that the low solubility of Ti precipitates, especially TiN, compared to AlN or NbC, is due to their low free energy of formation [23, 31]. It should be noted, however, that this can only be assumed under the equilibrium conditions. The behaviour of the precipitates during the rapid welding-temperature cycle must be considered separately. The high thermal stability of Ti precipitates limits the growth of austenite grains even at high temperatures or slower cooling rates [32]. This has a positive effect on the strength and toughness of the welded joint.

### 3.3.2 Non-equilibrium diagrams (module: TC-PRISMA)

For the simulation of the real precipitation behaviour during rapid cooling of the weld, a non-isothermal simulation for the non-equilibrium state was carried out (Fig. 9). For this purpose, experimentally determined cooling curves (Fig. 9a) were implemented in the TC-PRISMA module. Here, only the cooling curves of the cover layer were considered. Subsequently, only the cooling conditions of the HAZ areas were recorded, which were subject to extreme hardness differences: CGHAZ (Fig. 9b) and SCHAZ (Fig. 9c). To reduce the non-trivial simulation, the chemical composition was limited to the elements Fe, C, Cr, N, and Al for the reference grade, additionally Nb for the grade A and Ti for grade B. For all further simplification reasons, the pure precipitates of AlN, Nb/Ti(C,N) phases at grain boundaries were specifically considered as nucleation sites.

In the steel grade B (Ti-microalloyed) during cooling conditions in the CGHAZ, titanium carbonitrides do not dissolve at peak temperatures above 1200 °C. They remain small even during cooling from 1200 °C. Nevertheless, a decrease in the particle radius can be seen, which is due to the diffusion of carbon and nitrogen, so that the particle size decreases minimally, but then finally settles to a saturation level within a few seconds. The final calculated particle mean radius of the Ti(C,N) in the CGHAZ has the lowest value of 3.4E-10 m, in contrast to the other two steel grades. Furthermore, a relationship to the thermal stability of the precipitates can be seen. Thus, in contrast to Ti(C,N) in grade B (Ti-microalloyed), AlN precipitates
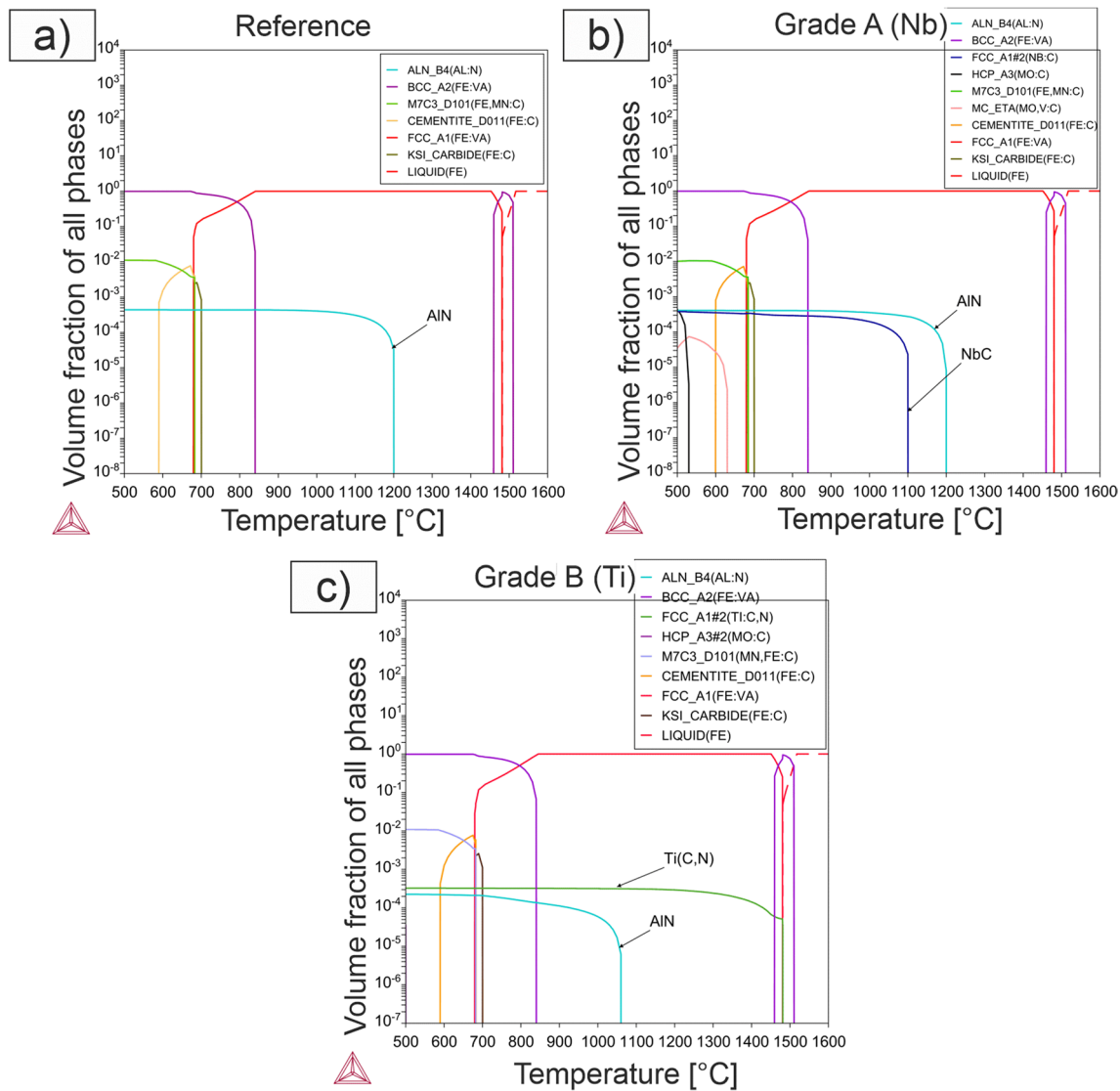
**Fig. 8** Equilibrium phase diagrams of investigated base materials: **(a)** reference grade, **(b)** grade A (Nb-microalloyed), and **(c)** grade B (Ti-microalloyed) S690QL

in the reference sample with a slightly larger particle mean radius of 3.8E-10 m, whereby the initial particle mean radius is the highest (6.6E-10 m) compared to the other two steels. In the steel grade A (Nb-microalloyed), larger NbC precipitates during the cooling process in contrast to AlN and Ti(C,N) precipitates. This can explain the different formation of the CGHAZ of the three steels investigated. Small finely distributed precipitates, like those of Ti(C,N) with a high thermal stability, hinder the austenite grain size by better pinning of the grain boundaries [33]. Furthermore, it can be suggested that the grain growth of the large grains is hindered by the smaller grains, which is also equivalent to a pinning effect. This would explain the narrower hardening zone in the CGHAZ of the top layer in grade B (Ti-microalloyed) steel.

In comparison, Fig. 9c shows the particle size as a function of the cooling conditions of the SCHAZ. This is the area where the softening zone is located. The peak temperature is 690 °C, and cooling is slower than in the CGHAZ. The mean particle radius of precipitates AlN, NbC, and Ti(C,N) in the SCHAZ is much smaller compared to that in the CGHAZ. It should be noted that these are precipitates with the nucleation sites at the grain boundaries in BCC matrix, which makes a direct comparison with the precipitation behaviour in the CGHAZ difficult. Both NbC and AlN precipitates show similar precipitation behaviour. The particle size before and after cooling remains almost constant, although diffusion processes take place in between. In contrast, Ti(C,N) precipitates show a different behaviour. Undissolved thermally stable Ti precipitates tend to reprecipitate, which can then be
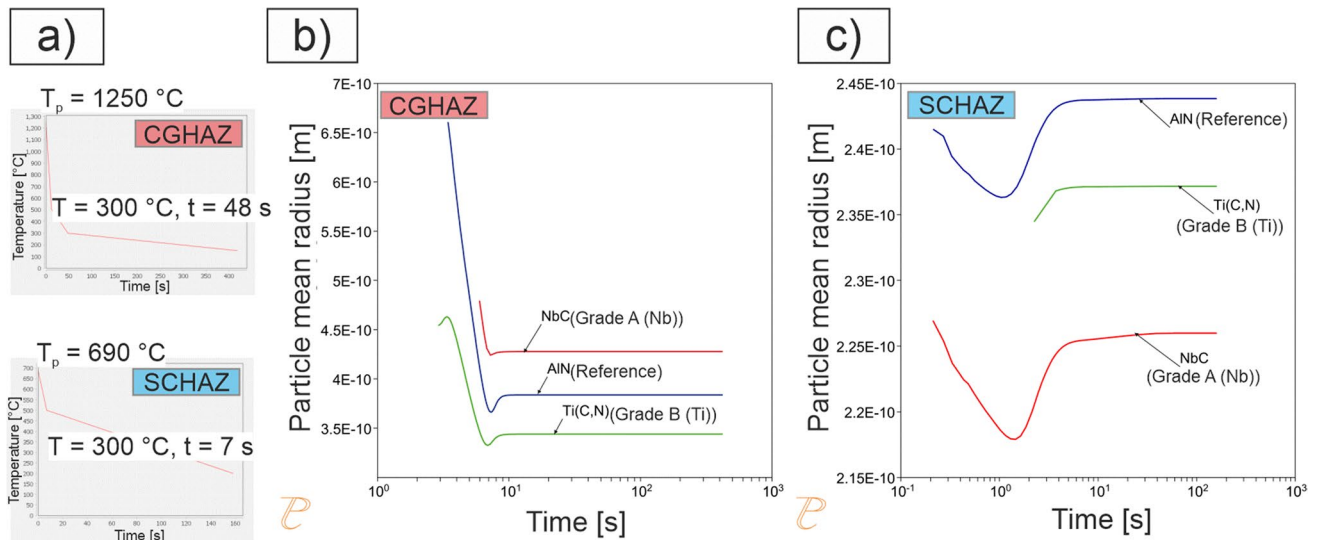
**Fig. 9** **(a)** Cooling profiles for the simulation of the precipitations, non-equilibrium diagrams for each of the three investigated steel grades: **(b)** particle size in CGHAZ vs. cooling time (FCC-matrix and nucleation site: grain boundary) and **(c)** particle size in SCHAZ vs. cooling time (BCC-matrix and nucleation site: grain boundary)

relatively coarse. Due to the different precipitate behaviour and different thermal stability of the precipitates, a divergent HAZ behaviour is to be expected.

## 4 Conclusions

The present study investigates the metallurgical aspects of the HAZ precipitation behaviour of welded and differently microalloyed grades of strength class S690QL. For that purpose, a Ti- and a Nb-alloyed grade was welded, and their microstructure and hardness were investigated. Further thermodynamic simulations were conducted to identify "in-situ" the precipitation characteristics. The following conclusions can be derived from the results presented:

- The UCI hardness distribution in the cross sections of the three-layer welded samples indicated that all investigated materials soften in the outer HAZ zones (ICHAZ and SCHAZ), although the softening intensity varies markedly between the investigated materials. It can be highlighted that the Ti-microalloyed steel grade showed a strong softening of the outer HAZ zones compared to the Nb-microalloyed grade
- The Nb-microalloyed steel grade shows significant resistance to tempering compared to the Ti-microalloyed grade. This can be explained by the interaction of Nb and the solid solution formers, such as the Mo. Large carbide clusters in the outer HAZ zones of the Nb-microalloyed steel grade were observed. Tempering

effects and a different phase distribution in the outer HAZ of the different microalloyed steel grades can explain these hardness differences
- Thermodynamic modelling with Thermo-Calc under equilibrium condition showed the high thermal stability of Ti precipitates. This has a positive influence on the pinning behaviour and the inhibition towards austenite grain growth. Non-isothermal simulation using TC PRISMA showed different time-dependent precipitation behaviour depending on the cooling conditions in both the CGHAZ and SCHAZ. The Ti-precipitates in the Ti-microalloyed steel do not dissolve entirely during the welding cycle. The particles show a kind of re-precipitation behaviour in the SCHAZ compared to the microalloyed Nb grade.

## Declarations

**Competing interests** The authors declare no competing interests.

## References

1. Abson D, Pargeter R (1986) Factors influencing as-deposited strength, microstructure, and toughness of manual metal arc welds suitable for C-Mn steel fabrications. Int Mater Rev 31(1):141–196. https://doi.org/10.1179/imtr.1986.31.1.141

2. Ahlblom B, Hansson P, Narström T (2007) Martensitic structural steels for increased strength and wear resistance. In: Materials science forum. Trans Tech Publications Ltd. https://doi.org/10.4028/www.scientific.net/MSF.539-543.4515

3. Hulka K, Kern A, Schriever U (2005) Application of niobium in quenched and tempered high-strength steels. In: Materials science forum. Trans Tech Publications Ltd. https://doi.org/10.4028/www.scientific.net/MSF.500-501.519

4. Mohrbacher H (2011) Mo and Nb alloying in plate steels for high-performance applications. In: International Symposium on the Recent Development in Plate Steels

5. Afkhami S et al (2022) Thermomechanical simulation of the heat-affected zones in welded ultra-high strength steels: microstructure and mechanical properties. Mater Des 213:110336. https://doi.org/10.1016/j.matdes.2021.110336

6. Baltazar Hernandez VH, Nayak SS, Zhou Y (2011) Tempering of martensite in dual-phase steels and its effects on softening behavior. Metall Mater Trans A 42(10):3115–3129. https://doi.org/10.1007/s11661-011-0739-3

7. Biro E et al (2010) Softening kinetics in the subcritical heat-affected zone of dual-phase steel welds. Metall Mater Trans A 41(9):2348–2356. https://doi.org/10.1007/s11661-010-0323-2

8. Biro E et al (2013) Predicting transient softening in the sub-critical heat-affected zone of dual-phase and martensitic steel welds. ISIJ Int 53(1):110–118. https://doi.org/10.2355/isijinternational.53.110

9. DIN EN 10025-6 (2020) Hot rolled products of structural steels – part 6: technical delivery conditions for flat products of high yield strength structural steels in the quenched and tempered condition. Beuth Verlag GmbH, Berlin

10. Zhang L, Kannengiesser T (2014) Austenite grain growth and microstructure control in simulated heat affected zones of microalloyed HSLA steel. Mater Sci Eng 613:326–335. https://doi.org/10.1016/j.msea.2014.06.106

11. Zhang L et al (2015) Effect of cooling rate on microstructure and properties of microalloyed HSLA steel weld metals. Sci Technol Weld 20(5):371–377. https://doi.org/10.1179/1362171815y.0000000026

12. Norrish J (2017) Recent gas metal arc welding (GMAW) process developments: the implications related to international fabrication standards. Weld World 61(4):755–767. https://doi.org/10.1007/s40194-017-0463-8

13. Zhang L, Kannengiesser T (2016) HAZ softening in Nb-, Ti- and Ti plus V-bearing quenched and tempered steel welds. Weld World 60(2):177–184. https://doi.org/10.1007/s40194-016-0299-7

14. DIN EN ISO 16834 (2012) Welding consumables – wire electrodes, wires, rods and deposits for gas shielded arc welding of high strength steels – classification (ISO 16834:2012). Beuth Verlag GmbH, Berlin

15. DIN 50159-1 (2022) Metallic materials – hardness testing with the UCI method – part 1: test method. Beuth Verlag GmbH, Berlin

16. DIN EN ISO 14175 (2008) Welding consumables – gases and gas mixtures for fusion welding and allied processes (ISO 14175:2008). Beuth Verlag GmbH, Berlin

17. DIN EN ISO 6507-1 (2018) Metallic materials – Vickers hardness test – part 1: test method (ISO 6507-1:2018). Beuth Verlag GmbH, Berlin

18. Andersson JO et al (2002) Thermo-Calc & DICTRA, computational tools for materials science. Calphad 26(2):273–312. https://doi.org/10.1016/S0364-5916(02)00037-8

19. Chen Q et al (2014) Modeling precipitation kinetics during heat treatment with CALPHAD-based tools. J Mater Eng Perform 23(12):4193–4196. https://doi.org/10.1007/s11665-014-1255-6

20. Saunders N, Miodownik AP (1998) CALPHAD (calculation of phase diagrams): a comprehensive guide. Elsevier

21. Gáspár M (2019) Effect of welding heat input on simulated HAZ areas in S960QL high strength steel. Metals 9(11):1226. https://doi.org/10.3390/met9111226

22. Chiew SP et al (2019) Experimental study of welding effect on S690Q high strength steel butt joints. ce/papers 3(3-4):701–706. https://doi.org/10.1002/cepa.1124

23. Easterling K (2013) Introduction to the physical metallurgy of welding. Elsevier

24. Baker TN (2016) Microalloyed steels. Ironmak 43(4):264–307. https://doi.org/10.1179/1743281215y.0000000063

25. Speich GR (1969) Tempering of low-carbon martensite. Trans Met Soc AIME 245(12):2553–2564

26. Komizo Y-I (2011) In-situ observation techniques of solidification and phase transformation during welding. Trans JWRI 40(2):7–20. https://doi.org/10.18910/6265

27. Egger R (2012) Herstellung und Eigenschaften von hochfesten, vergüteten Grobblechen. Berg- hüttenmänn Monatsh 157(8-9):332–339. https://doi.org/10.1007/s00501-012-0027-6

28. Zhang L (2017) Microstructure-property relationship in microalloyed high-strength steel welds, ed. B.D. (155). Eigenverlag Bundesanstalt für Materialforschung und-prüfing (BAM), Berlin

29. Villalobos JC et al (2018) Microalloyed steels through history until 2018: review of chemical composition, processing and hydrogen service. Metals 8(5):351. https://doi.org/10.3390/met8050351

30. Vervynckt S et al (2012) Modern HSLA steels and role of non-recrystallisation temperature. Int Mater Rev 57(4):187–207. https://doi.org/10.1179/1743280411y.0000000013

31. Schick HL (2013) Discussion of theoretical studies: Sections I-VI. Elsevier

32. Loberg B et al (1984) The role of alloy composition on the stability of nitrides in Ti-microalloyed steels during weld thermal cycles. Metall Mater Trans A Phys Metall Mater Sci 15(1):33–41. https://doi.org/10.1007/Bf02644385

33. Ion JC, Easterling KE, Ashby MF (1984) A second report on diagrams of microstructure and hardness for heat-affected zones in welds. Acta Metall 32(11):1949–1962. https://doi.org/10.1016/0001-6160(84)90176-7